

Improving Stability Margins with Grid-Forming Damper Winding Emulation

Dahlia Saba, Dominic Groß

Abstract—This work presents (i) a framework for certifying small-signal frequency stability of a power system with line dynamics and heterogeneous bus dynamics, (ii) a novel reduced-order model of damper windings in synchronous machines, and (iii) a proportional-derivative (PD) damper winding emulation control for voltage-source converters (VSCs). Damper windings have long been understood to improve the frequency synchronization between machines. However, the dynamics of the damper windings are complex, making them difficult to analyze and directly emulate in the control of VSCs. This paper derives a reduced-order model of the damper windings as a PD term that allows grid-forming controls for VSCs to emulate their effect on frequency dynamics. Next, a framework for certifying small-signal frequency stability of a network with heterogeneous bus dynamics is developed that extends prior results by incorporating line dynamics. Finally, we analytically demonstrate that PD damper winding emulation can improve the stability of grid-forming converter controls. These results are validated with electromagnetic-transient (EMT) simulation.

I. INTRODUCTION

CONVERTER-interfaced resources such as wind, solar photovoltaics, and battery energy storage have been rapidly deployed to bulk power systems. Existing deployments overwhelmingly use voltage source converters (VSCs) with grid-following control, which relies on the presence of conventional synchronous generators to ensure grid stability. Grid-forming (GFM) control has been proposed as an alternative that allows converter-based resources to operate grids without synchronous generators [1], [2]. Historically, stability analysis of bulk power systems has relied on the physical properties of synchronous machines, namely their inherently high rotational inertia and well-understood controls. Converter-interfaced resources lack these physical properties: VSCs have limited internal energy storage, giving them faster dynamics and lower inertia, and many more degrees of freedom in their controls. As a result, new analysis methods are needed to ensure the stability of bulk power systems that contain both synchronous machines and converter-based resources.

One significant difference between synchronous machines and converter-based resources is the presence of damper windings in machines, which help damp rotor oscillations [3], [4]. Existing works have proposed designing converter controls to emulate the effect of damper windings. One approach is to approximate the induced damping power with the difference between the estimated grid frequency and the converter frequency. Some works accomplish this by measuring the grid frequency with a phase-locked loop (PLL) [5], [6]; however, the PLL can cause instability, particularly in weak grids [7]. Other work adds a frequency damping term that effectively approximates the grid frequency with the nominal frequency [8],

but this model is inaccurate, leading to undesirable behavior if the grid frequency is not at its nominal value.

Other approaches emulate the effects of damper windings without estimating the grid frequency by adjusting the converter duty cycle [9], adjusting the output voltage amplitude [3], adding virtual flux variables [10], or using a transient virtual impedance [11]. However, the system-level impact of these controls is difficult to mathematically analyze. Therefore, while [3], [9]–[11] demonstrate stability benefits in small numerical studies, it is unclear how to tune these controls or if these effects generalize to larger systems.

Methods for certifying the stability of power systems with converter-interfaced resources in the literature generally fall into three categories: large-signal analytical conditions, small-signal analytical conditions, and small-signal numerical conditions. Large-signal stability criteria certify stability of the nonlinear power system dynamics, but typically only apply to networks of homogeneous converters (e.g., [12]). On the other hand, numerical small-signal analysis (e.g., impedance models [13]–[16] and eigenvalue sensitivity analysis [17]), which account for heterogeneous controls and circuit dynamics, require modeling the entire power system under study. Notably, their computational complexity often makes them impractical for analyzing large networks and results do not generalize to systems beyond the specific system under study.

Existing bus-level analytical small-signal stability conditions for networks of converter-interfaced resources with line dynamics are highly scalable [18]–[21]. Bus-level stability criteria have been derived for networks with droop-controlled converters in microgrids with heterogeneous resistance-to-reactance (R/X) ratios [18], droop-controlled converters in transmission networks with homogeneous line dynamics [21], and for proportional-derivative droop and frequency and angle droop [19]. These results all assume the network is solely composed of converters limited to one type of control, and thus are unable to account for instabilities that may arise in heterogeneous networks (e.g., interactions between a converter and a synchronous generator).

Fewer analytical works exist in the literature that certify stability for a network with heterogeneous bus dynamics that are not restricted to any particular control. A set of bus-level (i.e., decentralized) stability criteria is presented in [22], and [20] extends its results to account for the effects of line dynamics with a homogeneous R/X ratio. However, both of these results do not cover marginally stable bus dynamics, which rules out common devices such as synchronous condensers, static synchronous compensators, and many renewables operating at their maximum power point. In contrast, the conditions in [23] allow for marginally stable bus dynamics and a reduced-order

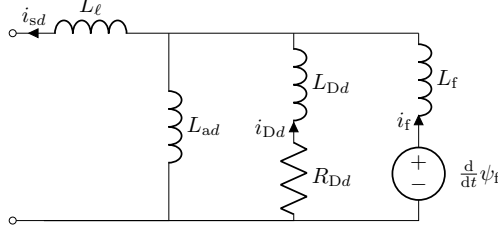


Fig. 1. Model of the d -axis synchronous machine circuit, where L_ℓ denotes the stator leakage inductance, L_{ad} denotes the d -axis magnetizing inductance, L_{Dd} and R_{Dd} denote the d -axis damper winding inductance and resistance, and L_f and ψ_f denote the field winding inductance and flux linkage. The q -axis circuit is modeled by replacing the field winding with an open circuit.

model damper winding model is introduced to demonstrate that synchronous condensers meet these conditions. However, the results of [23] do not cover line dynamics.

In this work, we provide a more rigorous justification of the damper winding model in [23], extending it to a network with line dynamics, and argue that the damper windings help stabilize both synchronous generators and condensers in the presence of line dynamics. Next, we develop a framework for certifying small-signal frequency stability of a power system with line dynamics and heterogeneous bus dynamics that relies on bus-level conditions and a few key system-level conditions. Moreover, we show that the reduced-order damper winding model can be emulated by converters using a proportional-derivative (PD) term. In contrast to other controls mimicking damper windings, the reduced-order damper winding emulation presented in this work is simple to implement and is shown to help stabilize system-level frequency dynamics even for large systems with heterogeneous bus dynamics. This provides physical intuition for the results of [19], which found that PD converter controls can compensate line dynamics in a system with homogeneous bus dynamics, and extends those results to systems with heterogeneous and marginally stable bus dynamics.

II. REDUCED-ORDER DAMPING TORQUE MODEL

In this section, we derive a reduced-order model of the impact of synchronous machine damper windings on the electrical torque near steady state. Let the electrical torque $\tau_e \in \mathbb{R}$ be expressed as

$$\tau_e = \tau_{\text{net}} + \tau_D, \quad (1)$$

where $\tau_{\text{net}} \in \mathbb{R}$ represents the torque corresponding to the active power injection into the grid and $\tau_D \in \mathbb{R}$ represents the torque induced by the damper windings. We show that the damping torque can be approximated by

$$\tau_D = \xi_{\text{SM}} \frac{d}{dt} \tau_{\text{net}}. \quad (2)$$

This derivation is based on the synchronous machine dynamic model presented in [24, Ch. 3, Ch. 5.3.2] and improves on the result from [23, Sec. 3]. In contrast to [23, Sec. 3], which assumes a multi-machine network in quasi-steady state without converters, this derivation applies to a machine connected to an arbitrary network which may have line dynamics.

Consider a synchronous machine with rotor angle $\theta_r \in [0, 2\pi)$ and a d -axis and a q -axis damper winding. It is assumed that the Canay inductance, stator resistance, and field winding resistance can be neglected. The equivalent circuit is shown in Fig. 1. Assuming all three-phase voltages and currents are balanced, we define a rotating dq -frame aligned with θ_r . Moreover, we define the 90° rotation matrix as

$$\mathbf{j} = \begin{bmatrix} 0 & -1 \\ 1 & 0 \end{bmatrix}.$$

Let $\psi_a = [\psi_{ad}, \psi_{aq}]^\top \in \mathbb{R}^2$ denote the air-gap flux linkage and $i_s = [i_{sd}, i_{sq}]^\top \in \mathbb{R}^2$ denote the stator current in dq -frame. Moreover, let $L_\ell \in \mathbb{R}_{\geq 0}$ denote the stator leakage inductance. The electrical torque $\tau_e \in \mathbb{R}$ can be expressed as

$$\tau_e = i_s^\top \mathbf{j} (\psi_a - L_\ell i_s) = i_s^\top \mathbf{j} \psi_a. \quad (3)$$

Let $\psi_D = [\psi_{Dd}, \psi_{Dq}]^\top \in \mathbb{R}^2$ denote the vector of flux linkages through the d - and q -axis damper windings and $\psi_f \in \mathbb{R}$ denote the field winding flux linkage. Likewise, let $L_{ad}, L_{aq} \in \mathbb{R}_{>0}$ denote the d - and q -axis magnetizing inductances, $L_{Dd}, L_{Dq} \in \mathbb{R}_{>0}$ denote the d - and q -axis damper winding inductances, and $L_f \in \mathbb{R}_{>0}$ denote the field winding inductance. The air gap flux linkage is given by $\psi_a = -L_a (-i_s + i_D + [i_f, 0]^\top)$, where $i_f \in \mathbb{R}$ is the field winding current. Moreover, the field winding flux linkage can be expressed as $\psi_f = \psi_{a,d} + L_f i_f$, and the damper winding flux linkage can be expressed as $\psi_D = \psi_a + L_D i_D$ [24, p. 188]. By defining the subtransient inductances $L''_{ad} := (L_{ad}^{-1} + L_f^{-1} + L_{Dd}^{-1})^{-1}$ and $L''_{aq} := (L_{aq}^{-1} + L_{Dq}^{-1})^{-1}$, the air-gap flux linkage can be expressed as

$$\psi_a = L''_a \left(-i_s + L_D^{-1} \psi_D + \frac{1}{L_f} \begin{bmatrix} \psi_f \\ 0 \end{bmatrix} \right), \quad (4)$$

where $L''_a := \text{diag}(L''_{ad}, L''_{aq}) \in \mathbb{R}^{2 \times 2}$ and $L_D := \text{diag}(L_{Dd}, L_{Dq}) \in \mathbb{R}^{2 \times 2}$. Substituting (4) into (3), we can express the electrical torque in the form of (1) as

$$\tau_e = \underbrace{\frac{L''_{ad}}{L_f} i_{sq} \psi_f + (L''_{aq} - L''_{ad}) i_{sd} i_{sq}}_{\tau_{\text{net}}} + \underbrace{i_s^\top \mathbf{j} L''_a L_D^{-1} \psi_D}_{\tau_D}. \quad (5)$$

To solve for ψ_D , we first solve for the damper winding currents, represented in dq coordinates by $i_D = [i_{Dd}, i_{Dq}]^\top \in \mathbb{R}^2$. The damper currents are given by

$$R_D i_D = -\frac{d}{dt} \psi_D, \quad (6)$$

where $R_D = \text{diag}(r_{Dd}, r_{Dq}) \in \mathbb{R}^{2 \times 2}$ is the matrix of damper winding resistances. Assuming the field winding flux is constant, substituting (4) into the expression for ψ_D and taking the derivative of both sides results in

$$\frac{d}{dt} \psi_D = L_D \frac{d}{dt} i_D + L''_a \left(-\frac{d}{dt} i_s + L_D^{-1} \frac{d}{dt} \psi_D \right),$$

which can be rewritten to obtain

$$\frac{d}{dt} \psi_D = (L_D - L''_a)^{-1} L_D \left(L_D \frac{d}{dt} i_D - L''_a \frac{d}{dt} i_s \right). \quad (7)$$

The damper windings act like the bars of an induction machine. We can therefore express the dynamics of the damping current in terms of the difference between the electrical frequency of the rotor and stator such that $\frac{d}{dt} i_D = (\omega_s - \omega_r) \mathbf{j} i_D$,

where $\omega_s \in \mathbb{R}$ is the stator frequency and $\omega_r \in \mathbb{R}$ is the rotor frequency. Moreover, if we assume the stator current has constant magnitude, we can express its dynamics in the rotating frame as $\frac{d}{dt}i_s = (\omega_s - \omega_r)\mathbf{j}i_s$. Using these expressions, we can substitute (7) into (6) to obtain

$$R_D i_D = -(\omega_s - \omega_r)(L_D - L_a'')^{-1} L_D (L_D \mathbf{j} i_D - L_a'' \mathbf{j} i_s).$$

Solving for i_D and linearizing around $\omega_s = \omega_r$ results in

$$i_D = (\omega_s - \omega_r) R_D^{-1} (L_D - L_a'')^{-1} L_D L_a'' \mathbf{j} i_s. \quad (8)$$

Neglecting any coupling between the field winding and damper winding fluxes, the damper winding flux linkage can now be expressed as

$$\begin{aligned} \psi_D &= -L_a i_s + L_D i_D \\ &= (-L_a + (\omega_s - \omega_r) R_D^{-1} (L_D - L_a'')^{-1} L_D^2 L_a'' \mathbf{j}) i_s. \end{aligned}$$

Substituting this into the damping torque in (5) results in

$$\begin{aligned} \tau_D &= -i_s^\top \mathbf{j} L_a'' L_D^{-1} L_a i_s + \\ &\quad i_s^\top \mathbf{j} (\omega_s - \omega_r) R_D^{-1} (L_D - L_a'')^{-1} L_D L_a''^2 \mathbf{j} i_s. \end{aligned}$$

Because the stator is predominantly inductive and voltages magnitudes are assumed to be at their nominal value, the current will be close to 90° out of phase with the rotor voltage in steady state conditions. As a result, we evaluate the expression at the point $i_s = [0, i_{sq}]^\top$, and τ_D reduces to

$$\tau_D = -(\omega_s - \omega_r) \frac{L_{Dd} L_{ad}''^2}{R_{Dd} (L_{Dd} - L_{ad}'')} i_{sq}^2. \quad (9)$$

Now consider the derivative of τ_{net} . Using $\frac{d}{dt}i_s = (\omega_s - \omega_r)\mathbf{j}i_s$, and assuming $\frac{d}{dt}\psi_f = 0$, it holds that

$$\frac{d}{dt} \tau_{\text{net}} = (\omega_s - \omega_r) [L_{ad}'' i_{sd} \psi_f + (L_{aq}'' - L_{ad}'') (i_{sd}^2 - i_{sq}^2)].$$

We again evaluate this expression at the operating point $i_{sd} = 0$. This gives the desired result (2), where ξ_{SM} is given by

$$\xi_{\text{SM}} := \frac{L_{Dd} L_{ad}''^2}{R_{Dd} (L_{Dd} - L_{ad}'') (L_{aq}'' - L_{ad}'')}. \quad (10)$$

This model is validated via EMT simulation in Sec. III-C.

III. POWER SYSTEM MODEL

This section presents the model used to analyze the bulk power system. First, the network power flow model is introduced, including second-order line dynamics. Then, dynamic models are presented for buses with converters and with synchronous machines, which are modeled as transfer functions from power to frequency. For synchronous machines, the transfer function incorporates the reduced-order damper winding model from Sec. II. Finally, the full frequency domain model of the interconnected system is introduced.

A. Dynamic small-signal Power Flow Model

Let the transmission network be modeled by a graph where \mathcal{N}_{tot} is the set of nodes corresponding to the buses and $\mathcal{E}_{\text{tot}} \subseteq \mathcal{N}_{\text{tot}} \times \mathcal{N}_{\text{tot}}$ is the set of edges corresponding to the transmission lines. Transmission lines are modeled as a series inductance and resistance. The dynamics of the current flowing across a line $(n, k) \in \mathcal{E}_{\text{tot}}$ are therefore described in dq -frame by

$$\ell_{nk} \frac{d}{dt} \begin{bmatrix} i_{nk,d} \\ i_{nk,q} \end{bmatrix} = \begin{bmatrix} -r_{nk} & \omega_0 \ell_{nk} \\ -\omega_0 \ell_{nk} & -r_{nk} \end{bmatrix} \begin{bmatrix} i_{nk,d} \\ i_{nk,q} \end{bmatrix} + \begin{bmatrix} v_{n,d} - v_{k,d} \\ v_{n,q} - v_{k,q} \end{bmatrix}$$

where $i_{nk,d}$ and $i_{nk,q}$ are the dq components of the line current, $v_{n,d}$ and $v_{n,q}$ are the dq components of the voltage at bus n , $v_{k,d}$ and $v_{k,q}$ are the dq components of the voltage at bus k , r_{nk} and ℓ_{nk} are respectively the line's resistance and inductance, and ω_0 is the nominal system frequency.

Let V_n and V_k be the magnitudes and θ_n and θ_k be the phase angles of the voltage waveforms at buses n and k respectively. By linearizing around the operating point $V_n = V_k = V^*$ and $\theta_n = \theta_k$, we can express the dynamics of the power p_{nk} flowing along the line (n, k) in frequency domain as

$$p_{nk}(s) = \frac{V^{*2}}{\omega_0 \ell_{nk}} \frac{\omega_0^2}{s^2 + 2 \frac{r_{nk}}{\ell_{nk}} s + (\frac{r_{nk}}{\ell_{nk}})^2 + \omega_0^2} (\theta_n(s) - \theta_k(s)). \quad (11)$$

For simplicity, we assume all lines in the network have the same resistance-reactance ratio.

Assumption 1 (Uniform R/X ratio) *The resistance-reactance ratio $\rho = \frac{r_{nk}}{\omega_0 \ell_{nk}}$ is the same for all $(n, k) \in \mathcal{E}_{\text{tot}}$.*

With this assumption, we can express $p_{nk}^{\text{pu}}(s)$, the per-unit power flowing across line (n, k) , as

$$p_{nk}^{\text{pu}}(s) = \frac{1}{\ell_{nk}^{\text{pu}}} \mu(s) (\theta_n(s) - \theta_k(s)),$$

where ℓ_{nk}^{pu} is the per-unit inductance of line (n, k) and $\mu(s)$ is the transfer function given by

$$\mu(s) := \frac{\omega_0^2}{s^2 + 2\omega_0\rho s + \omega_0^2(1 + \rho^2)}.$$

We define the vector $p_{\text{net}}^{\text{tot}}(s) \in \mathbb{C}^{|\mathcal{N}_{\text{tot}}|}$ such that $p_{\text{net},n}^{\text{tot}}(s)$ represents the per-unit net power injected into the network at bus n . The total network power injections are expressed by

$$p_{\text{net}}^{\text{tot}}(s) = \mu(s) L_{\text{tot}} \theta_{\text{tot}}(s),$$

where $\theta_{\text{tot}}(s) \in \mathbb{C}^{|\mathcal{N}_{\text{tot}}|}$ is the vector of voltage phase angles at each bus and $L_{\text{tot}} \in \mathbb{R}^{|\mathcal{N}_{\text{tot}}| \times |\mathcal{N}_{\text{tot}}|}$ is the Laplacian matrix constructed from the graph $(\mathcal{N}_{\text{tot}}, \mathcal{E}_{\text{tot}})$ where each edge $(n, k) \in \mathcal{E}_{\text{tot}}$ has weight $(\ell_{nk}^{\text{pu}})^{-1}$. The network is Kron-reduced [25] to only the nodes $\mathcal{N} \subseteq \mathcal{N}_{\text{tot}}$ corresponding to buses with generation and energy storage resources. $\mathcal{E} \subseteq \mathcal{N} \times \mathcal{N}$ denotes the edges of the reduced network. The power flow for the reduced network can be expressed by

$$p_{\text{net}}(s) = \mu(s) L \theta(s), \quad (12)$$

where $p_{\text{net}}(s) \in \mathbb{C}^{|\mathcal{N}|}$, $L \in \mathbb{R}^{|\mathcal{N}| \times |\mathcal{N}|}$ and $\theta(s) \in \mathbb{C}^{|\mathcal{N}|}$ respectively denote the vector of net power injections, the Laplacian matrix, and the vector of voltage phase angles corresponding to the reduced network.

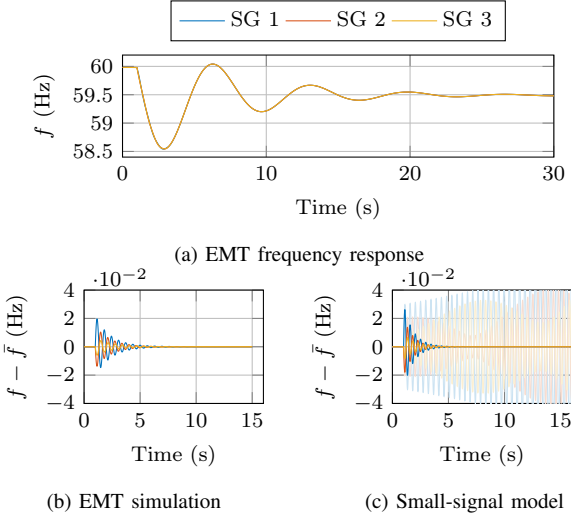


Fig. 2. The small-signal system model, using the synchronous generator model (14) and line model (12) is compared to an EMT simulation of the IEEE 9-bus model after a load step of 0.5 p.u. at Bus 7. Incorporating the damper winding model allows the small-signal model to capture the frequency synchronization between the machines (dark lines in (c)), which a swing equation model without damper windings (faint lines in (c)) cannot capture.

B. Converter Model

A grid-connected converter at a bus $n \in \mathcal{N}$ can be modeled by the transfer function

$$g_n(s) := \frac{\omega_n(s)}{p_n(s)},$$

where $\omega_n(s)$ is the frequency of the AC voltage imposed by the converter and $p_n(s)$ is the per-unit power imbalance at the converter bus, expressed in Laplace domain.

C. Model of Synchronous Machine with Damper Windings

The frequency dynamics of a machine at bus $n \in \mathcal{N}$ can be described by

$$\frac{2H_n}{\omega_0} \frac{d}{dt} \omega_n = P_{\text{gen},n} - P_{\text{load},n} - P_{\text{net},n} - P_{\text{D},n} \quad (13a)$$

where H_n denotes the machine's inertia constant, ω_n denotes the difference between the rotor frequency and the nominal system frequency, $P_{\text{gen},n}$ denotes the mechanical power generation, $P_{\text{load},n}$ denotes the power consumed by load at bus n , $P_{\text{net},n}$ denotes the power injected into the network at bus n , and $P_{\text{D},n}$ denotes the damping power induced by the machine damper winding, where all powers are expressed as per-unit quantities. If the machine is a generator with a turbine-governor system, the mechanical power generation follows

$$T_{G,n} \frac{d}{dt} P_{\text{gen},n} = -P_{\text{gen},n} - \frac{k_{g,n}}{\omega_0} \omega_n, \quad (13b)$$

where $T_{G,n}$ is the turbine time constant and $k_{g,n}$ is the per-unit governor gain; for a synchronous condenser $P_{\text{gen},n} = 0$.

Under the assumption that ω_n changes relatively slowly, we can approximate $P_{\text{D},n} = \xi_{\text{SM},n} \frac{d}{dt} P_{\text{net},n}$ with the reduced-order damper winding model derived in Sec. II, i.e., $\xi_{\text{SM},n}$ given

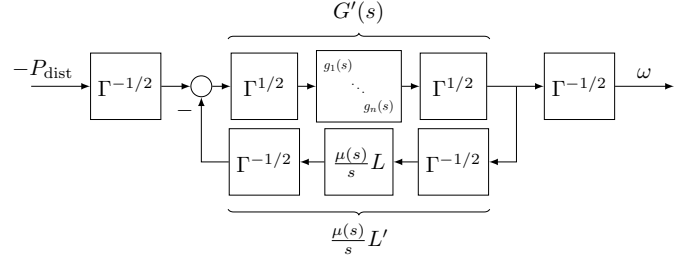


Fig. 3. Block diagram of the normalized small-signal power system model. The normalized bus dynamics are represented by $G'(s)$ and the normalized power flow model is represented by $\frac{\mu(s)}{s} L'$.

by (10) and the parameters of the machine at bus n . As a result, we can express (13a) in frequency domain as

$$\frac{2H_n}{\omega_0} \omega_n s = P_{\text{gen},n} - P_{\text{load},n} - (1 + \xi_{\text{SM},n} s) P_{\text{net},n}.$$

Accounting for the turbine-governor dynamics (13b), the dynamics of a synchronous generator can be written as

$$\omega_n = \frac{\omega_0(1 + \xi_{\text{SM},n} s)(1 + T_{G,n} s)}{2H_n T_{G,n} s^2 + 2H_n s + k_{g,n}} \left(-\frac{P_{\text{load},n}}{1 + \xi_{\text{SM},n} s} - P_{\text{net},n} \right).$$

We define $P_{\text{dist},n} := P_{\text{load},n}/(1 + \xi_{\text{SM},n} s)$. The transfer function from $-(P_{\text{dist},n} + P_{\text{net},n})$ to frequency for a synchronous generator can then be expressed as

$$g_{\text{SG}}(s) = \frac{\omega_0(1 + \xi_{\text{SM},n} s)(1 + T_{G,n} s)}{2H_n T_{G,n} s^2 + 2H_n s + k_g}. \quad (14)$$

For synchronous condensers, we derive the transfer function

$$g_{\text{SC}}(s) = \frac{\omega_0(1 + \xi_{\text{SM},n} s)}{2H_n s}.$$

Comparing the small-signal model of the IEEE 9-bus system [26, p. 38] to an EMT simulation shows that adding the reduced-order damper winding model significantly improves the ability of the small-signal machine model to capture the frequency synchronization dynamics (Fig. 2). In fact, if the damper winding model is excluded from the small-signal model, the interactions between the line dynamics and the machine model are unstable.

D. Closed-loop Frequency Domain Model

We define the power disturbance vector $P_{\text{dist}} \in \mathbb{C}^{|\mathcal{N}|}$ such that $P_{\text{dist},n} = P_{\text{load},n}/(1 + \xi_n s)$ if $n \in \mathcal{N}$ is a bus with a synchronous machine and $P_{\text{dist},n} = P_{\text{load},n}$ otherwise. The power system dynamics can be described by the negative feedback interconnection between the matrix of bus dynamic transfer functions $G(s) = \text{diag}\{g_n(s)\}_{n \in \mathcal{N}}$ and the power flow matrix $\frac{\mu(s)}{s} L$, where the input to the system is P_{dist} and the output is the frequency ω . If the total transfer function from P_{load} to ω is the cascade of two stable systems, it must be stable. Thus, it suffices to check the stability of the transfer function from P_{dist} to ω to show stability of the full system.

Assumption 2 For every bus $n \in \mathcal{N}$, $g_n(s)$ can be expressed as a rational proper transfer function with real coefficients.

Define $\gamma_n := 2 \sum_{(n,k) \in \mathcal{E}} 1/\ell_{nk}^{\text{pu}}$ and $\Gamma := \text{diag}\{\gamma_n\}_{n \in \mathcal{N}}$. Then, we can rescale by Γ as shown in Fig. 3 to express the system as the feedback interconnection between $G'(s) := \Gamma^{1/2}G(s)\Gamma^{1/2}$ and $\mu(s)/sL'$, where $L' := \Gamma^{-1/2}L\Gamma^{-1/2}$. Note that $\text{spec}\{L'\} \in [0, 1]$ [22, Lemma 1] and $G'(s)$ is a diagonal matrix where the n -th entry $g'_n(s)$ is equal to the bus dynamics $g_n(s)$ rescaled by the susceptances of local lines.

IV. STABILITY ANALYSIS

The stability of the frequency dynamics in Fig. 3 is analyzed in Sec. IV-A by first considering the slow dynamics where the bus dynamics cohere to the synchronous system dynamics. Subsequently, we consider the faster dynamics where interactions between bus dynamics dominate the system response. This analysis results in a set of stability criteria, which are further decomposed into several timescales in Sec. IV-B to interpret the requirements for different frequency ranges. Section IV-C discusses the application of these conditions.

A. Stability Criteria

Following [27] we define the synchronous dynamics

$$\bar{g}(s) := \left(\frac{1}{|\mathcal{N}|} \sum_{n \in \mathcal{N}} (g'_n)^{-1}(s) \right)^{-1}. \quad (15)$$

Moreover, let $S_\delta = \{s \in \overline{\mathbb{C}}_+ : |s| < \delta\}$ for some $\delta \in \mathbb{R}_{>0}$, where $\overline{\mathbb{C}}_+$ denotes the closed right-half complex plane, and let $\lambda_2(L')$ denote the second-smallest eigenvalue of L' .

Condition 1 (Stable synchronous & coherent dynamics)

The synchronous dynamics $\bar{g}(s)$ of the system satisfy

1) for all $s \in \overline{\mathbb{C}}_+$, $|\bar{g}(s)| \leq M_1$ for some $M_1 \in \mathbb{R}_{>0}$.

Moreover, for some $\delta \in \mathbb{R}_{>0}$, the following hold for all $s \in S_\delta$:

2) there exists $M_2 \in \mathbb{R}_{>0}$ such that $\max_{n \in \mathcal{N}} |(g'_n)^{-1}(s)| \leq M_2$,

3) $\left| \frac{s}{\mu(s)} \right| < \frac{\lambda_2(L')}{M_2 + M_1 M_2^2}$.

Condition 1.1 ensures that the synchronous dynamics $\bar{g}(s)$ are stable. Moreover, by [27, Lemma 1], Conditions 1.2 and 1.3 ensure that, for slow dynamics (i.e., $s \in S_\delta$), the system response will be incrementally stable with respect to the synchronous dynamics (i.e., the deviation of the system response from the synchronous response is bounded), which can be interpreted as the system response cohering to the synchronous dynamics near steady-state. Therefore, Condition 1 ensures that the system will have a stable response to slow perturbations within the region S_δ in the Laplace domain. Note that if Conditions 1.1 and 1.2 are satisfied, there always exists a small enough δ such that Condition 1.3 is satisfied over S_δ .

Condition 2 (Stable synchronizing dynamics) For a given $\delta \in \mathbb{R}_{>0}$, the following conditions hold for all $n \in \mathcal{N}$:

1) $g'_n(s)$ does not have any poles in $\overline{\mathbb{C}}_+ \setminus S_\delta$,
2) there exists a function $\alpha : \mathbb{C} \rightarrow (0, \pi/2]$ such that

$$\Re \left\{ e^{j(\pi/2 - \alpha(s))} \left(1 + \frac{\mu(s)}{s} g'_n(s) \right) \right\} > 0$$

for all $n \in \mathcal{N}$ and all s on the boundary of $\overline{\mathbb{C}}_+ \setminus S_\delta$.

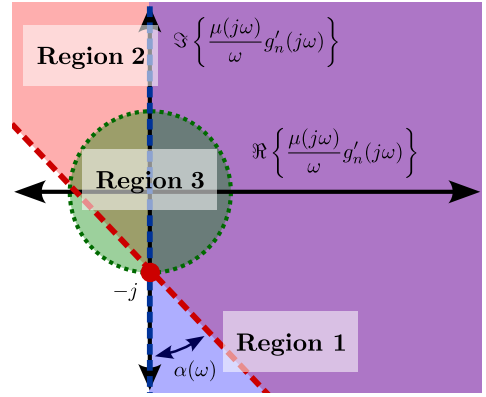


Fig. 4. The interoperability regions in Condition 3 are shown on the complex plane. Region 1 is shaded in blue, Region 2 in red, and Region 3 in green.

Condition 2.1 ensures that each $g_n(s)$ does not have any unstable poles outside of the coherent region S_δ . Condition 2.2 ensures the interoperability of the bus dynamics by ensuring that for a given s , all $\frac{\mu(s)}{s} g'_n(s)$ must lie in a fixed half plane given by $\alpha(s)$. A more interpretable sufficient condition for Condition 2.2 is presented in Sec. IV-B.

Theorem 1 (Frequency stability) Consider a connected Kron-reduced network with uniform R/X ratio $\rho > 0$. If there exists $\delta > 0$ such that Conditions 1 and 2 are satisfied, the interconnected system in Fig. 3 is internally stable.

A proof is presented in the Appendix.

B. Understanding Interoperability Condition

In this section we introduce and analyze Condition 3, a more interpretable sufficient condition for satisfying Condition 2.2.

Condition 3 (Interpretable interoperability condition) For some $\delta \in \mathbb{R}_{>0}$, some $\omega_1, \omega_2 \in \mathbb{R}_{>0}$ where $\omega_2 \geq \omega_1 \geq \delta$, and some function $\alpha : [\omega_1, \omega_2] \rightarrow (0, \pi/2]$, the following conditions hold for all $n \in \mathcal{N}$:

Region 1: for all $s \in \{\delta e^{j\theta} : \theta \in [0, \pi/2]\} \cup \{j\omega : \omega \in [\delta, \omega_1]\}$, it holds that $\Re(\mu(s)g'_n(s)) > 0$

Region 2: for all $\omega \in [\omega_1, \omega_2]$, one of the following conditions holds true:

- $\angle \mu(j\omega)g'_n(j\omega) \in (-\pi/2 + \alpha(\omega), \pi/2 - \alpha(\omega))$
- $\left| \frac{\mu(j\omega)}{\omega} g'_n(j\omega) \right| < \frac{\sin \alpha(\omega)}{|\cos(\angle \mu(j\omega)g'_n(j\omega) - \alpha(\omega))|}$

Region 3: for all $\omega \in [\omega_2, \infty]$, $\left| \frac{\mu(j\omega)}{\omega} g'_n(j\omega) \right| < 1$ holds.

These regions, depicted in Fig. 4, can be understood as requiring small phase (Region 1), small gain (Region 3), or some tradeoff between the two (Region 2). We first consider Regions 1 and 3, which can be interpreted as letting $\alpha(s)$ in Condition 2.2 approach 0 and $\pi/2$, respectively.¹ Region 1 requires each $g_n(s)\mu(s)$ to have positive real part for low frequencies, which means each $g_n(s)\mu(s)$ must dissipate energy at these frequencies. It also requires $g_n(s)\mu(s)$ to have

¹Note that α still remains strictly greater than zero in Region 1, satisfying $\alpha \in (0, \pi/2]$. Condition 2.1 requires $g'_n(s)$ to have finite gain, ensuring that if $\Re(\mu(s)g'_n(s)) > 0$, we can always select $\alpha > 0$ to satisfy Condition 2.2.

positive real part on the set $s \in \{\delta e^{j\theta} : \theta \in [0, \pi/2]\}$, but Assumption 2 ensures this can always be satisfied for small enough δ if $\Re(g_n(j\delta)\mu(j\delta)) > 0$. Region 3 requires each $g_n(s)\mu(s)$ to have small gain at high frequencies, where a more connected node (i.e., large γ_n) has a stricter gain limit.

Region 2, the medium frequency region, allows $\alpha(s)$ to take a value between those extremes, trading off the phase and gain conditions on $g'_n(s)\mu(s)$. If the phase satisfies $\angle\mu(j\omega)g'_n(j\omega) \in (-\pi/2 + \alpha(\omega), \pi/2 - \alpha(\omega))$, $g'_n(s)$ will satisfy the interoperability requirements for mid-range frequencies. If $g'_n(s)$ does not satisfy this phase requirement, it can satisfy the second condition of Region 2, which imposes a gain limit that grows tighter as the phase of $\mu(j\omega)g'_n(j\omega)$ grows further outside of the range $(-\pi/2 + \alpha(\omega), \pi/2 - \alpha(\omega))$. If the gain satisfies $\left|\frac{\mu(j\omega)}{\omega}g'_n(j\omega)\right| < \sin \alpha(\omega)$, the requirement will be satisfied for any phase of $\mu(j\omega)g'_n(j\omega)$. Note that if $g'_n(s)$ satisfies $\Re(\mu(j\omega)g'_n(j\omega)) > 0$ and $\left|\frac{\mu(j\omega)}{\omega}g'_n(j\omega)\right| < 1$ (i.e., satisfies the conditions from both Regions 1 and 3), the condition from Region 2 will always be satisfied.

C. Application of Interoperability Condition

We now discuss how Condition 3 can be used for stability analysis, defining a topology-independent relative stability margin to aid in its application. Condition 3 requires that for every bus, the function $g_n(s)\mu(s)$ must either have positive real part (i.e., dissipate energy) or have gain less than ω/γ_n at each frequency. Generally, the 180° phase shift induced by the line dynamics will cause $\Re(g_n(j\omega)\mu(j\omega))$ to become negative for many common bus models. As a result, for a bus n with dynamics $g_n(s)$, we define the crossover frequency $\omega_c^n := \min\{\omega : \omega \in \mathbb{R}_{\geq 0}, \angle g_n(j\omega)\mu(j\omega) = -90^\circ\}$. In a system with homogeneous bus dynamics, ω_c^n will be the same for all $n \in \mathcal{N}$, and by setting $\omega_1 = \omega_2 = \omega_c$, Condition 3 reduces to a condition that each $g'_n(s)$ satisfies $\left|\frac{1}{\omega}\mu(j\omega)g'_n(j\omega)\right| < 1$ for all $\omega \geq \omega_c$. For a heterogeneous system, we define $\omega_1 \leq \min_{n \in \mathcal{N}} \omega_c^n$ and $\omega_2 \geq \max_{n \in \mathcal{N}} \omega_c^n$. Then, in Region 2, $\alpha(\omega)$ can be set to trade off between the strictness of the phase and the gain conditions: a larger $\alpha(\omega)$ corresponds to a less restrictive gain condition at the expense of a tighter phase bound for buses that do not meet the gain condition, and vice versa. However, for any choice of $\alpha(\omega)$, every bus $n \in \mathcal{N}$ must satisfy $\left|\frac{\mu(j\omega_c^n)}{\omega_c^n}g'_n(j\omega_c^n)\right| < 1$. We can therefore define

$$M(g, \mu) := \frac{\omega_c}{\left|\mu(j\omega_c)g(j\omega_c)\right|},$$

as the relative stability margin, where $\left|\frac{\mu(j\omega_c^n)}{\omega_c^n}g'_n(j\omega_c^n)\right| < 1$ will be satisfied if $M(g_n, \mu) > \gamma_n$. Figure 5 shows a sample Bode plot of $\frac{1}{\omega}\mu(j\omega)g(j\omega)$ for a synchronous machine where the crossover frequency ω_c and the relative stability margin $M(g_{SG}, \mu)$ are visualized.

V. EFFECT OF DAMPER WINDING MODEL ON SYNCHRONOUS MACHINE STABILITY

This section examines the application of Condition 3 to synchronous machine models in a system with line dynamics.

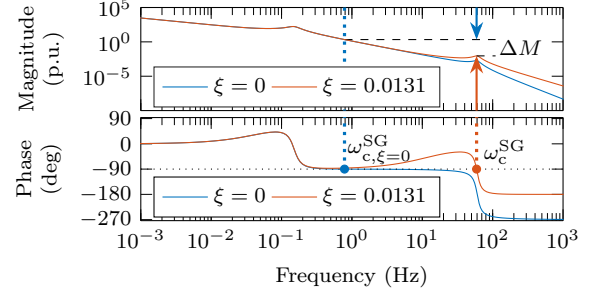


Fig. 5. The Bode plot of $\frac{1}{\omega}\mu(j\omega)g(j\omega)$ is shown for a 60 Hz system where $\rho = 0.1$ and $g(j\omega) = g_{SG}(j\omega)$ with $H = 3.7$, $T_G = 3$, and $k_g = 20$. The transfer function is plotted with no damper winding model (i.e. $\xi_{SM} = 0$) and with $\xi_{SM} = 0.0131$. The crossover frequency ω_c^{SG} for each value of ξ_{SM} is indicated on the phase plot, and ΔM on the magnitude plot depicts the increased stability margin for $\xi_{SM} = 0.0131$.

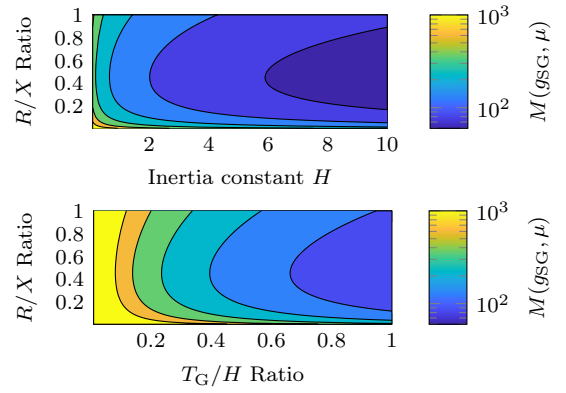


Fig. 6. The relative stability margin of a synchronous machine is shown over a range of machine parameters and system R/X ratios. Above, the margin is shown as a function of the inertia constant H while the ratio T_G/H of the turbine time constant to the inertia constant is fixed at 0.8. Below, the margin is shown as a function of T_G/H while for H fixed at 3s.

Notably, including the reduced-order damper winding model can improve the stability of synchronous machine models even in cases when increasing machine inertia hurts stability.

A. Synchronous Generators

Using the framework from Sec. III-C, the bus dynamics of synchronous generators are modeled by (14). For small enough δ , $\mu(\delta e^{j\theta})g_{SG}(\delta e^{j\theta})$ will have positive real part for any $\theta \in [-\pi/2, \pi/2]$. Moreover, $\mu(j\omega)g_{SG}(j\omega)$ will have positive real part for small ω . However, the phase shift induced by the line dynamics will cause $\mu(j\omega)g_{SG}(j\omega)$ to have negative real part at higher frequencies. For a synchronous generator at bus n , Condition 3 requires that $M(g_{SG}, \mu) > \gamma_n$ and that $\frac{1}{\omega}|\mu(j\omega)g_{SG}(j\omega)| < \gamma_n^{-1}$ holds for all $\omega > \omega_c^{SG}$, where ω_c^{SG} is the crossover frequency of the bus dynamics. Therefore, if ω_c^{SG} is less than the line dynamic resonant frequency $\omega_r := \omega_0\sqrt{1 - \rho^2}$, a potential local maximum of the transfer function, we must also verify that $\frac{1}{\omega_r}|\mu(j\omega_r)g_{SG}(j\omega_r)| < \gamma_n^{-1}$.

By including the reduced-order damper winding model in $g_{SG}(s)$ (i.e., $\xi_{SM} > 0$), we can increase the relative stability margin. The damper winding model adds an additional zero to $g_{SG}(s)$, lifting the phase by 90° . If $\xi_{SM} > (\omega_0\sqrt{1 + \rho^2})^{-1}$,

ω_c^{SG} will move towards $\omega_0\sqrt{1+\rho^2}$, the natural frequency of the line dynamics. To understand the impact of the reduced-order damper winding model, we will compare the relative stability margin of $g_{\text{SG}}^{\xi=0}(s)$, the synchronous generator transfer function without the damper winding model, to the margin of $g_{\text{SG}}(s)$ with the damper winding model (i.e., $\xi_{\text{SM}} > 0$).

First, we approximate $M(g_{\text{SG}}^{\xi=0}, \mu)$. Let $\omega_{c,\xi=0}^{\text{SG}}$ denote the crossover frequency of the model when the damper windings are excluded. Note that while $\omega_{c,\xi=0}^{\text{SG}}$ cannot easily be expressed in closed form, it can be numerically computed for a given bus and will always lie between the poles of $g_{\text{SG}}(s)$ and $\mu(s)$. By invoking timescale separation between the synchronous machine dynamics and the line dynamics, we assume that $\omega_{c,\xi=0}^{\text{SG}} \gg \sqrt{k_g/2HT_{\text{G}}}$, allowing us to approximate $|g_{\text{SG}}(j\omega_{c,\xi=0}^{\text{SG}})| \approx \omega_0/(2H\omega_{c,\xi=0}^{\text{SG}})$. Similarly, we assume $\omega_{c,\xi=0}^{\text{SG}} \ll \omega_0\sqrt{1+\rho^2}$ to obtain $|\mu(j\omega_{c,\xi=0}^{\text{SG}})| \approx 1/(1+\rho^2)$. Therefore, we can approximate the stability margin as

$$M(g_{\text{SG}}^{\xi=0}, \mu) \approx \frac{2H(1+\rho^2)(\omega_{c,\xi=0}^{\text{SG}})^2}{\omega_0}. \quad (16)$$

Remark 1 Increasing the inertia constant H moves the poles of $g_{\text{SG}}(s)$ to lower frequencies, thereby decreasing $\omega_{c,\xi=0}^{\text{SG}}$. As a result, despite H appearing in the numerator of (16), increasing the inertia may lower $M(g_{\text{SG}}^{\xi=0}, \mu)$ (see Fig. 6).

To conservatively estimate the effect of the damper winding model, we compare $M(g_{\text{SG}}^{\xi=0}, \mu)$ to $M(g_{\text{SG}}, \mu)$ if ξ_{SM} moves ω_c^{SG} to $\omega_r = \omega_0\sqrt{1-\rho^2}$. Invoking timescale separation again, we approximate $g(j\omega_c^{\text{SG}}) \approx \xi_{\text{SM}}\omega_0/(2H)$ and $\mu(j\omega_c^{\text{SG}}) = 1/2\rho$, resulting in the conservative estimate

$$M(g_{\text{SG}}, \mu) \approx \frac{4H\rho\sqrt{1-\rho^2}}{\xi_{\text{SM}}}. \quad (17)$$

Comparing (17) to (16), we estimate that incorporating the damper winding model will improve the stability margin if

$$(\omega_0\sqrt{1+\rho^2})^{-1} < \xi_{\text{SM}} < \frac{2\rho\omega_0\sqrt{1-\rho^2}}{(\omega_{c,\xi=0}^{\text{SG}})^2(1+\rho^2)}. \quad (18)$$

This range aligns with typical values of ξ_{SM} for transmission-connected generators. An example is shown in Fig. 5.

Note that the upper bound depends heavily on the network R/X ratio: if ρ approaches zero, the damper winding model will not improve the stability margin of the system. Thus, the damper windings can be understood to help compensate for the phase lag induced by line losses. The bound is also inversely proportional to $(\omega_{c,\xi=0}^{\text{SG}})^2$, suggesting that damper windings have greater stability benefits for machines with more inertia.

B. Synchronous Condensers

If $\xi_{\text{SM}} = 0$, $g_{\text{sc}}(j\omega)$ will be purely imaginary for all ω . Because $\mu(j\omega)$ induces a negative phase shift, this means that $\Re(\mu(j\omega)g_{\text{sc}}(j\omega)) \leq 0$. Furthermore, for small ω , the gain of $g_{\text{sc}}(j\omega)$ becomes very large, so unless the network is very weakly connected (i.e., γ is very small), the synchronous condenser will not satisfy either the phase or the gain condition at low frequencies if $\xi_{\text{SM}} = 0$. However, $\xi_{\text{SM}} > 0$ will induce a positive phase shift that, if ξ_{SM} is large enough, makes

$\Re(\mu(j\omega)g_{\text{sc}}(j\omega)) > 0$ for low frequencies where $g_{\text{sc}}(j\omega)$ does not meet the small gain requirement. Therefore, modeling the effect of damper windings is necessary for demonstrating the stability of synchronous condensers in this framework.

VI. EMULATING DAMPER WINDINGS THROUGH CONVERTER CONTROL

The stabilizing effects of damper windings in machines can be achieved in converter-interfaced resources by incorporating a PD term to emulate the reduced-order damper winding model. This can provide significant stability improvements over more conventional droop/VSM control, particularly in networks with a larger R/X ratio. This section generalizes the results of [19] to a network with heterogeneous bus dynamics and presents a physical interpretation of PD droop control as emulating the effects of damper windings for converters.

Compared with other damper winding emulation strategies [3], [9]–[11], PD droop control is significantly simpler, allowing us to analytically model the effect of the damper winding emulation in a system with heterogeneous generation. Emulating the reduced-order damper winding model rather than the full model also has performance advantages. Because damper windings are essentially induction machines, they may destabilize the frequency dynamics if the slip between rotor and stator frequencies becomes too large. In contrast, the reduced-order PD model only models the stabilizing linear region of the damper windings, i.e., effectively emulates only the stabilizing effects of the damper windings.

A. Conventional Droop Control

Conventional filtered droop control can be expressed as

$$g_{\text{dr}}(s) = \frac{m_p\omega_0}{T_p s + 1},$$

where m_p is the per-unit droop coefficient and T_p is the filter time constant. Note that this is equivalent to VSM control: $g_{\text{dr}}(s)$ matches (14) if $T_{\text{G}} = 0$, $\xi_{\text{SM}} = 0$, and $T_p = 2H/k_g$.

Let ω_c^{dr} denote the frequency at which $\Re(\mu(j\omega)g_{\text{dr}}(j\omega))$ crosses from positive to negative. We can express ω_c^{dr} as a function of T_p by solving $\Re(\mu(j\omega)g_{\text{dr}}(j\omega)) < 0$ for ω , which we can equivalently find by solving for the ω where $\Re(\mu^{-1}(j\omega)g_{\text{dr}}^{-1}(j\omega)) < 0$. This expression becomes

$$\begin{aligned} 0 &> \Re(\mu^{-1}(j\omega)g_{\text{dr}}^{-1}(j\omega)) \\ &> -\omega^2 - 2T_p\rho\omega_0\omega^2 + \omega_0^2(1+\rho^2), \end{aligned}$$

and we find that $\Re(\mu(j\omega)g_{\text{dr}}(j\omega))$ becomes negative at

$$\omega_c^{\text{dr}} = \omega_0 \sqrt{\frac{1+\rho^2}{1+2\rho\omega_0 T_p}}.$$

With this expression for ω_c^{dr} , the condition $M(g_{\text{dr}}, \mu) > \gamma_n$ is equivalent to the stability condition for a network of homogeneous droop-controlled VSCs [19, Eq. (10)]. The stability criteria derived here therefore replicate the results from [19] concerning the potential instability of droop control: namely, that stabilizing droop control by tuning the virtual inertia may not always be possible, or might require infeasibly large values

of T_p . To ensure these dynamics also meet our interoperability requirements, we must also ensure that any gain increase caused by the resonant peak does not result in instability: i.e., if $\omega_c^{\text{dr}} < \omega_r$, it must also hold that $\frac{1}{\omega_r} |\mu(j\omega_r)g_{\text{dr}}(j\omega_r)| < \gamma_n^{-1}$. Rewriting this condition, we can equivalently conclude that if $T_p > \rho/(\omega_0(1 - \rho^2))$, then it must hold that

$$T_p > \frac{\sqrt{\gamma_n^2 m_p^2 - 4\rho^2(1 - \rho^2)}}{2\rho(1 - \rho^2)\omega_0}. \quad (19)$$

However, increasing T_p beyond this bound may not necessarily result in better performance, as increasing T_p can reduce ω_c^{dr} to a frequency with a higher gain.

B. PD Droop Control as Damper Winding Emulation

To improve the stability of droop control, we augment $g_{\text{dr}}(s)$ to mimic the reduced-order damper winding model with the PD term $(1 + \xi_C s)$ for $\xi_C \in \mathbb{R}_{>0}$, resulting in PD droop control

$$g_{\text{pd}}(s) = \frac{m_p \omega_0 (1 + \xi_C s)}{T_p s + 1}.$$

Note that while $g_{\text{pd}}(s)$ is not realizable for $T_p = 0$, it can still be implemented in a VSC because the transfer function for the angle, given by $\frac{1}{s}g_{\text{pd}}(s)$, is realizable. Notably, dual-port GFM control [28] with a curtailed resource matches the form of $g_{\text{pd}}(s)$ [19]. As with synchronous machines, ξ_C provides a phase lift that increases ω_c at the expense of increasing $|g(s)|$. In particular, if $\xi_C > (\omega_0 \sqrt{1 + \rho^2})^{-1}$, its phase lift will partially compensate the phase drop from $\mu(s)$, increasing ω_c .

We can estimate the range of parameters for which adding $\xi_C > 0$ improves the performance of droop control. VSCs have faster dynamics than machines, so we can no longer assume timescale separation with the line dynamics. However, if

$$M(g_{\text{dr}}, \mu) < \frac{\omega}{\left| \mu(j\omega)g_{\text{dr}}(j\omega) \left(1 + \frac{j\omega}{\omega_0 \sqrt{1 + \rho^2}} \right) \right|} \quad (20)$$

holds for all $\omega > \omega_c^{\text{dr}}$, increasing ω_c by setting $\xi_C \geq (\omega_0 \sqrt{1 + \rho^2})^{-1}$ can increase the relative stability margin, despite it also increasing $|g(s)|$. Note that the natural frequency of $\mu(s)$ is given by $\omega_n = \omega_0 \sqrt{1 + \rho^2}$. To approximate the parameters for which (20) holds for $\omega > \omega_c^{\text{dr}}$, we evaluate the inequality at the potential local maximum ω_r . This reduces (20) to the condition that

$$\Xi := (1 + 2\rho\omega_0 T_p)^2 - \sqrt{\frac{2\omega_n^2 (T_p^2 \omega_n^2 + 2\rho\omega_0 T_p + 1)^2}{\omega_r^2 (T_p^2 \omega_r^2 + 1)}}$$

must be positive. A larger Ξ indicates that ξ_C can increase the stability margin further. Figure 7 plots Ξ over a range of ρ and T_p , showing that adding a non-zero derivative term ξ_C can achieve the most substantial stability gains for devices with larger inertia ratios in more resistive networks. However, Ξ is still positive except for very small ρ or T_p , showing that incorporating $\xi_C > 0$ can improve the stability margin for VSCs in most typical operating scenarios (e.g., Fig. 8).

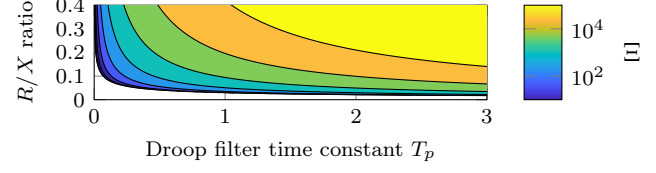


Fig. 7. Ξ is plotted over various R/X ratios and virtual inertia values, with the graph left blank if the value is negative.

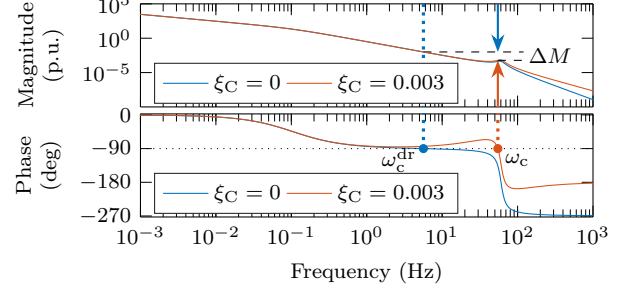


Fig. 8. The Bode plot of $\frac{1}{\omega} \mu(j\omega)g(j\omega)$ is shown for a 60 Hz system where $\rho = 0.1$ and $g(j\omega) = g_{\text{pd}}(j\omega)$ with $T_p = 1.5$. The crossover frequency ω_c for each value of ξ_C is indicated on the phase plot, and ΔM on the magnitude plot depicts the increased stability margin for $\xi_C = 0.003$.

VII. CASE STUDY: VSC PLANT

We validate the analytical stability conditions by performing an EMT simulation of a modified IEEE 9-bus system where one of the generators is replaced by a VSC plant. We also demonstrate the stability benefits of the reduced-order damper winding emulation control presented in Sec. VI.

A. Simulation Setup

The system (Fig. 9) is simulated in MATLAB Simulink using Simscape Electrical. The simulation lasts for two minutes, with an 0.5 p.u. load step at Bus 7 after 30 seconds. The line parameters have varying R/X ratios that, treating stator and transformer impedances as lines, range from $\rho_{\min} = 0.0304$ to $\rho_{\max} = 0.2294$. The synchronous generators are salient-pole machines with droop turbine-governor systems. Each machine also uses an IEEE type ST1A voltage regulator and exciter and a multiband power system stabilizer.

The VSC plant is composed of eight two-level converters, each represented by an averaged VSC model. Each converter

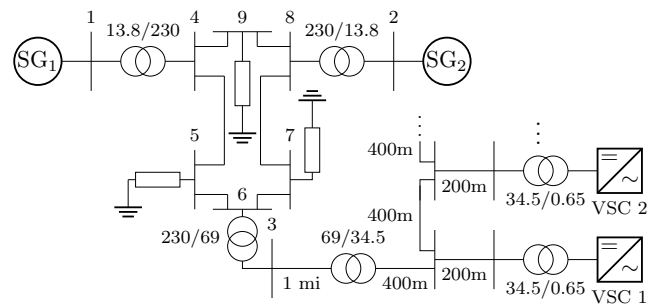


Fig. 9. The modified IEEE 9-bus system with a VSC plant added at Bus 3.

TABLE I
PARAMETERS OF THE SIMULATED SYSTEM.

System base values					
S_b	100 MVA	v_b	230 kV	ω_b	$2\pi 60 \text{ rad/s}$
Synchronous generator (SG)					
S_r	100 MVA	v_r	13.8 kV	P^*	75 W
H	3.7 s	k_g	20 p.u.	T_G	3 s
L_{Dd}	0.182 p.u.	R_{Dd}	0.0117 p.u.	L''_{ad}	0.0662 p.u.
L''_{aq}	0.1858 p.u.				
SG MV/HV transformer					
S_r	210 MVA	v_1	13.8 kV	v_2	230 kV
$R_1 = R_2$	0.00338 p.u.	$L_1 = L_2$	0.1 p.u.	$R_m = L_m$	500 p.u.
VSC Plant MV/HV transformer					
S_r	210 MVA	v_1	69 kV	v_2	230 kV
$R_1 = R_2$	0.00338 p.u.	$L_1 = L_2$	0.1 p.u.	$R_m = L_m$	500 p.u.
VSC Plant MV/MV transformer					
S_r	120 MVA	v_1	34.5 kV	v_2	69 kV
$R_1 = R_2$	0.00125 p.u.	$L_1 = L_2$	0.05 p.u.	$R_m = L_m$	500 p.u.
VSC Plant LV/MV transformer					
S_r	13.32 MVA	v_1	34.5 kV	v_2	0.65 kV
$R_1 = R_2$	0.003 p.u.	$L_1 = L_2$	0.025 p.u.	$R_m = L_m$	500 p.u.
VSC Parameters					
S_r	13.32 MVA	v_r	0.65 kV	P^*	9.375 W
v_{DC}^*	2.76 kV	k_{DC}	35.03	C_{DC}	0.008 F
VSC Plant Line Parameters (Pi Line Model)					
200m R	66 $\mu\Omega/\text{m}$	200m L	0.43 $\mu\text{H}/\text{m}$	200m C	$2.4 \times 10^{-5} \mu\text{F}/\text{m}$
400m R	20 $\mu\Omega/\text{m}$	400m L	0.37 $\mu\text{H}/\text{m}$	400m C	$2.8 \times 10^{-5} \mu\text{F}/\text{m}$
1 mi R	0.3076 Ω	1 mi L	1.8 mH	1 mi C	$1.593 \times 10^{-8} \mu\text{F}$

is attached to its own DC generation, which is represented as a controlled current source with a current i_{DC} depends on its voltage v_{DC} such that $i_{DC} = P^*/v_{DC}^* + k_{DC}(v_{DC}^* - v_{DC})$, where P_{DC}^* and v_{DC}^* are the active power and DC voltage setpoints and $k_{DC} \in \mathbb{R}_{\geq 0}$ represents the generation response to DC voltage deviations. This model mimics the small-signal response of curtailed solar PV and battery energy storage systems. The outer converter controls are implemented using nested proportional-integral current and voltage loops. The parameters for the VSC plant lines and transformers are adapted from [29]. The complete system parameters are listed in Table I.

B. Results with Conventional Droop Control

First, we analyze the system if all converters implement conventional droop control. The outer controls are modeled by $g_{dr}(s)$ with $m_p = 0.05$ and $T_p = 3\text{s}$, which satisfy the lower bound given by (19) and fall within the range of commonly suggested parameters for battery energy storage systems. Note that Assumption 1 is not satisfied for this system, and the line R/X ratios range from ρ_{\min} to ρ_{\max} . However, we can still apply the analytical stability criteria by analyzing stability for both $\mu(s)$ defined with ρ_{\min} and $\mu(s)$ defined with ρ_{\max} .

Applying the individual analytical requirements to each converter, we see that this control results in potentially unstable behavior (Fig. 10). In particular, for higher R/X ratios, $M(g_{dr}, \mu) < \gamma_n$ is not satisfied for nodes n within the VSC plant. Moreover, while the condition appears satisfied for lower R/X ratios (i.e., $\frac{1}{\omega}|\mu(j\omega)g'(j\omega)| < 1$ when $\angle\mu(j\omega)g'(j\omega) \notin (-90^\circ, 90^\circ)$), the phase plot for $\frac{1}{\omega}\mu(j\omega)g'_{dr}(j\omega)$ is very flat around -90° . This means that slight changes to the phase response could reduce ω_c to an unstable value, indicating a lack of robustness to unmodeled dynamics.

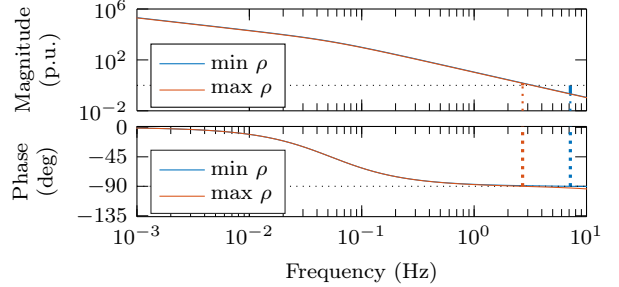


Fig. 10. Bode plot of $\frac{1}{\omega}\mu(j\omega)g'(j\omega)$ for VSC 4 with bus dynamics $g_{dr}(s)$ where $m_p = 5\%$ and $T_p = 3\text{s}$. The plot is shown for $\mu(s)$ with R/X ratios 0.0304 and 0.2294, the minimum and maximum system values. The vertical dotted lines correspond to ω_c for each transfer function, and the solid vertical lines on the magnitude plot denote the magnitude at ω_c . For the maximum ρ , the gain at ω_c is greater than 1, indicating potential instability.

In EMT simulation, these control values lead to an unstable system response (Fig. 12), resulting in a growing oscillation between the frequency responses of VSCs within the plant. The oscillation has frequency of approximately 1.7 Hz, which is close to the instability around 2.7 Hz suggested by the Bode plot in Fig. 10. We speculate that the frequency discrepancy is due to the sensitivity of the crossover frequency of VSC droop control to dynamics in the simulated system that are not captured in the small-signal model.

C. Results with PD Damper Winding Emulation

Next, we control each converter with PD damper winding emulation $g_{pd}(s)$ with $\xi_C = 0.005$, where again $m_p = 0.05$ and $T_p = 3\text{s}$. This increases ω_c for the converters to near line frequency, where the gain of the frequency response is much smaller. As a result, the converters in the VSC plant have a much larger stability margin across the range of R/X values. Plotting the frequency response of the converters and the machines on the same axes (Fig. 11) reveals there is now a significant frequency range (3.3 Hz – 54.0 Hz) for which the converters and machines all have both positive real part and gain less than one. Therefore, we can certify interoperability via Condition 3 with $\omega_1 = 3.3 \text{ Hz}$ and $\omega_2 = 54 \text{ Hz}$.

The improved analytical stability margin translates to improved performance in simulation. The system is able to maintain stability throughout the full 2 minute simulation (Fig. 12). Notably, the frequency oscillations observed within the VSC plant with conventional droop are well-damped with the PD droop control. This enhanced frequency convergence matches the effect of incorporating the reduced-order damper winding model into the synchronous machine model for multi-machine systems demonstrated in Fig. 2c.

VIII. CONCLUSION

This paper presented a reduced-order model of damper windings that improved the small-signal model of synchronous machines. The paper also introduced a set of decentralized conditions for ensuring the small-signal frequency stability of a system with heterogeneous bus dynamics and homogeneous line dynamics. With these stability conditions, it was shown

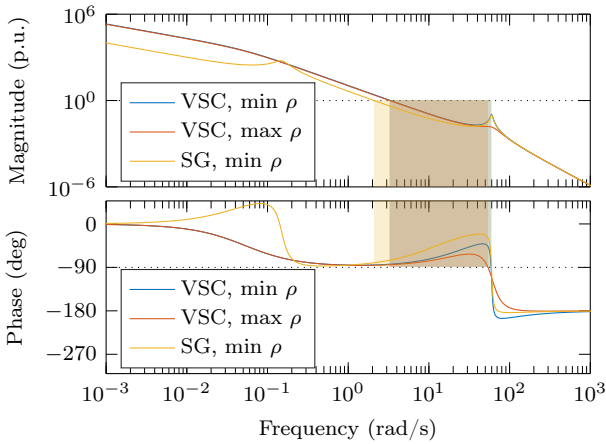


Fig. 11. Bode plot of $\frac{1}{\omega} \mu(j\omega) g'(j\omega)$ is shown for a synchronous machine and a converter in the modified 9-bus system when the converter dynamics are given by $g_{pd}(s)$ with $m_p = 5\%$, $\xi_C = 0.005$ and $T = 3$. The plot for the inverter is shown for the minimum and maximum system R/X ratios. Each Bode plot is shaded with its corresponding color over the frequency range where $\Re(\frac{1}{\omega} \mu(j\omega) g'(j\omega)) > 0$ and $|\frac{1}{\omega} \mu(j\omega) g'(j\omega)| < 1$. The overlap of these shaded regions, shown in brown, corresponds to Region 2 in Condition 3.

that incorporating the reduced-order damper winding model improves the stability margin of synchronous machines under common operating conditions. Further, this paper showed that PD droop control for converters can be interpreted as emulating the synchronizing effect of damper windings, and the presented stability conditions were used to demonstrate the stability benefits of PD droop control over conventional droop control. Finally, the advantages of PD droop control were demonstrated in an EMT simulation.

The analysis presented here only demonstrated small-signal stability, so while it is a good approximation of transmission line dynamics, it cannot capture the full nonlinear dynamics of the power system. Additionally, this model neglects the AC voltage magnitude and reactive power dynamics. This paper also neglected the DC bus dynamics and excluded high voltage DC lines. Developing stability criteria for the dynamics of AC voltage magnitude and DC voltage is seen as an interesting direction of future work. Other areas of future work include incorporating robustness margins into the stability criteria to account for model inaccuracies (e.g., nonlinearity and heterogeneous R/X ratios).

APPENDIX

PROOF OF THEOREM 1

Proof. By [30, Thm 4.12], showing that the transfer function $H(s) := \left(I + G'(s) \frac{\mu(s)}{s} L' \right)^{-1} G(s)$ is stable guarantees the internal stability of the closed loop system in Fig. 3 if no poles in $\overline{\mathbb{C}}_+$ are canceled between $G'(s)$ and $\frac{\mu(s)}{s} L'$. This requirement is satisfied by Conditions 1.1 and 1.2. Because Condition 1.1 ensures the synchronous dynamics have no unstable poles, the kernel of L' , given by $\text{span}(\mathbb{1}_n)$, cannot cancel out any unstable poles. Condition 1.2 implies that $G'(s)$ has no zeros at the origin, so it will not cancel the $\frac{1}{s}$ term in $\frac{\mu(s)}{s} L'$. Finally, because $\rho > 0$, all poles of $\mu(s)$ are stable.

To prove the stability of $H(s)$, we show that $|H(s)|$ is bounded over $s \in \overline{\mathbb{C}}_+$. By [27, Thm 3], Condition 1 guarantees that the system will converge to $\bar{g}(s)$ in steady state. Moreover, Condition 1.1 ensures that the coherent dynamics will have bounded magnitude over $s \in S_\delta$. We can further assert that for $s \in S_\delta$, $|H(s)|$ will be a finite distance from $|\bar{g}(s)|$ [27, Lemma 1], ensuring $|H(s)|$ is bounded over $s \in S_\delta$.

To prove stability over $s \in \overline{\mathbb{C}}_+ \setminus S_\delta$, we adapt the arguments used in [22] and [20, Thm 1]. Condition 2.1 implies that each $g'_n(s)$ will be analytic in the interior of $\overline{\mathbb{C}}_+ \setminus S_\delta$, so by the maximum modulus principle, we can show $|H(s)|$ is bounded over $\overline{\mathbb{C}}_+ \setminus S_\delta$ by showing that $|H(s)|$ is bounded over the boundary of the set. Because by Condition 2.1 $|G'(s)|$ is bounded in $\overline{\mathbb{C}}_+ \setminus S_\delta$, $|H(s)|$ is bounded on $\overline{\mathbb{C}}_+ \setminus S_\delta$ if and only if zero is not an eigenvalue of $I + G'(s) \frac{\mu(s)}{s} L'$ for all s on the boundary of $\overline{\mathbb{C}}_+ \setminus S_\delta$. Applying the logic of [22, Thm. 1], it is sufficient to show that $0 \notin \text{Co} \left(\left\{ 1 + k \frac{\mu(s)}{s} g'_n(s) : n \in \mathcal{N}, 0 \leq k \leq 1 \right\} \right)$ for all s on the boundary of $\overline{\mathbb{C}}_+ \setminus S_\delta$, where Co denotes the convex hull of a set. Applying the separating hyperplane principle, this is satisfied for a given s if and only if there exists some angle $\phi \in [0, \pi/2)$ such that $\Re \left(e^{j\phi} \left(1 + \frac{\mu(s)}{s} g'_n(s) \right) \right) > 0$ for all $n \in \mathcal{N}$. Condition 2.2 guarantees that this holds all s on the boundary of $\overline{\mathbb{C}}_+ \setminus S_\delta$. \square

REFERENCES

- [1] J. Matevosyan, B. Badrzadeh, T. Prevost, E. Quitmann, D. Ramasubramanian, H. Urdal, S. Achilles, J. MacDowell, S. H. Huang, V. Vital, J. O'Sullivan, and R. Quint, "Grid-Forming Inverters: Are They the Key for High Renewable Penetration?" *IEEE Power and Energy Magazine*, vol. 17, no. 6, pp. 89–98, Nov. 2019.
- [2] R. H. Lasseter, Z. Chen, and D. Pattabiraman, "Grid-Forming Inverters: A Critical Asset for the Power Grid," *IEEE J. Emerg. Sel. Top. Power Electron.*, vol. 8, no. 2, pp. 925–935, 2020.
- [3] M. Ebrahimi, S. A. Khajehoddin, and M. Karimi-Ghartemani, "An Improved Damping Method for Virtual Synchronous Machines," *IEEE Trans. Sustain. Energy*, vol. 10, no. 3, pp. 1491–1500, Jul. 2019.
- [4] X. Zhao, X. Kestelyn, and D. Flynn, "Transient stability analysis and modelling of systems with grid-forming converters and synchronous generators," in *Renewable Power Generation and Future Power Systems Conference*, Nov. 2023, pp. 198–207.
- [5] F. Gao and M. R. Iravani, "A Control Strategy for a Distributed Generation Unit in Grid-Connected and Autonomous Modes of Operation," *IEEE Trans. Power Del.*, vol. 23, no. 2, pp. 850–859, Apr. 2008.
- [6] T. Shintai, Y. Miura, and T. Ise, "Oscillation Damping of a Distributed Generator Using a Virtual Synchronous Generator," *IEEE Trans. Power Del.*, vol. 29, no. 2, pp. 668–676, Apr. 2014.
- [7] D. Dong, B. Wen, D. Boroyevich, P. Mattavelli, and Y. Xue, "Analysis of Phase-Locked Loop Low-Frequency Stability in Three-Phase Grid-Connected Power Converters Considering Impedance Interactions," *IEEE Trans. Ind. Electron.*, vol. 62, no. 1, pp. 310–321, Jan. 2015.
- [8] Q.-C. Zhong and G. Weiss, "Syncronverters: Inverters That Mimic Synchronous Generators," *IEEE Trans. Ind. Electron.*, vol. 58, no. 4, pp. 1259–1267, Apr. 2011.
- [9] I. Cvetkovic, D. Boroyevich, R. Burgos, C. Li, and P. Mattavelli, "Modeling and control of grid-connected voltage-source converters emulating isotropic and anisotropic synchronous machines," in *Workshop on Control and Modeling for Power Electronics*, 2015.
- [10] H. Yin, Z. Kustanovich, and G. Weiss, "Attenuation of power system oscillations by using virtual damper windings," in *Workshop on Control and Modeling for Power Electronics*, 2022.
- [11] P. M. Gajare, J. Benzaquen, and D. Divan, "Grid-Forming Controller with Enhanced Disturbance Rejection," *IEEE J. Emerg. Sel. Top. Power Electron.*, 2025.
- [12] D. Groß, M. Colombino, J.-S. Brouillon, and F. Dörfler, "The Effect of Transmission-Line Dynamics on Grid-Forming Dispatchable Virtual Oscillator Control," *IEEE Trans. Control Netw. Syst.*, vol. 6, no. 3, pp. 1148–1160, 2019.

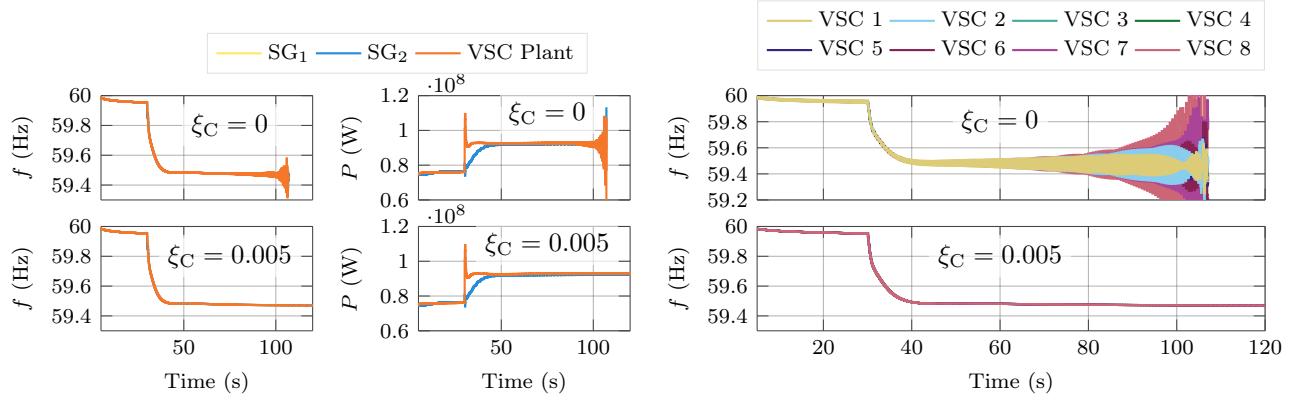


Fig. 12. EMT simulation results for frequencies (left) and power injections (middle) at the high voltage buses and individual VSC frequencies (right) using conventional droop control (i.e., $\xi_C = 0$, shown in top row) and PD droop control (i.e., $\xi_C = 0.005$, bottom row). Using conventional droop control, an unstable frequency oscillation occurs in the VSC plant. In contrast, the PD droop control is able to damp that oscillation and maintain stability of the system.

- [13] M. Cespedes and J. Sun, "Impedance Modeling and Analysis of Grid-Connected Voltage-Source Converters," *IEEE Trans. Power Electron.*, vol. 29, no. 3, pp. 1254–1261, Mar. 2014.
- [14] L. Harnefors, X. Wang, A. G. Yepes, and F. Blaabjerg, "Passivity-Based Stability Assessment of Grid-Connected VSCs—An Overview," *IEEE J. Emerg. Sel. Top. Power Electron.*, vol. 4, no. 1, pp. 116–125, Mar. 2016.
- [15] K. Yu, Q. Ai, S. Wang, J. Ni, and T. Lv, "Analysis and Optimization of Droop Controller for Microgrid System Based on Small-Signal Dynamic Model," *IEEE Trans. Smart Grid*, vol. 7, no. 2, pp. 695–705, Mar. 2016.
- [16] Y. Liao, X. Wang, F. Liu, K. Xin, and Y. Liu, "Sub-Synchronous Control Interaction in Grid-Forming VSCs with Droop Control," in *IEEE Workshop on the Electronic Grid*, 2019.
- [17] N. Pogaku, M. Prodanovic, and T. C. Green, "Modeling, analysis and testing of autonomous operation of an inverter-based microgrid," *IEEE Trans. Power Electron.*, vol. 22, no. 2, pp. 613–625, 2007.
- [18] P. Vorobev, P.-H. Huang, M. Al Hosani, J. L. Kirtley, and K. Turitsyn, "A framework for development of universal rules for microgrids stability and control," in *IEEE Conference on Decision and Control*, 2017, pp. 5125–5130.
- [19] D. Groß, "Compensating Network Dynamics in Grid-Forming Control," in *Annual Allerton Conference on Communication, Control, and Computing*, Monticello, IL, USA, 2022.
- [20] J. T. Bui and D. Groß, "Input-Output Specifications of Grid-Forming Functions and Data-Driven Verification Methods," 2024, arXiv:2404.15951 [eess].
- [21] V. Häberle, X. He, L. Huang, F. Dörfler, and S. Low, "Decentralized Parametric Stability Certificates for Grid-Forming Converter Control," Jun. 2025, arXiv:2503.05403 [eess].
- [22] R. Pates and E. Mallada, "Robust Scale-Free Synthesis for Frequency Control in Power Systems," *IEEE Trans. Control Netw. Syst.*, vol. 6, no. 3, pp. 1174–1184, Sep. 2019.
- [23] D. Saba and D. Groß, "Frequency Domain Stability Conditions for Hybrid AC/DC Systems," *Sustainable Energy, Grids and Networks*, 2025, Art. no. 101852.
- [24] P. Kundur, *Power System Stability and Control*. McGraw-Hill, 1994.
- [25] F. Dörfler and F. Bullo, "Kron Reduction of Graphs With Applications to Electrical Networks," *IEEE Trans. Circuits Syst. I*, vol. 60, no. 1, pp. 150–163, Jan. 2013.
- [26] Paul M. Anderson and Abdel-Aziz A. Fouad, *Power System Control and Stability*, 1st ed. Ames, Iowa: The Iowa State University Press, 1977.
- [27] H. Min, R. Pates, and E. Mallada, "A frequency domain analysis of slow coherency in networked systems," *Automatica*, vol. 174, 2025, Art. no. 112184.
- [28] I. Subotić and D. Groß, "Universal Dual-Port Grid-Forming Control: Bridging the Gap Between Grid-Forming and Grid-Following Control," *IEEE Trans. Power Syst.*, vol. 39, no. 6, pp. 6861–6875, Nov. 2024.
- [29] D. Ramasubramanian, "GFM Plant Architecture Unit level vs Plant level performance requirements," Jul. 2025, presentation.
- [30] S. Skogestad and I. Postlethwaite, *Multivariable Feedback Control - Analysis and design*, 2nd ed. John Wiley & Sons, 2005.